nanomaterials

MDPI

Article

Novel Ag-Bridged Z-Scheme CdS/Ag/Bi_2WO_6 Heterojunction: Excellent Photocatalytic Performance and Insight into the Underlying Mechanism

Fangzhi Wang *, Lihua Jiang, Guizhai Zhang, Zixian Ye, Qiuyue He, Jing Li, Peng Li, Yan Chen, Xiaoyan Zhou and Ran Shang

School of Resources and Environmental Engineering, Shandong Agriculture and Engineering University, Jinan 250100, China; jiangli8227@sina.com (L.J.); zgzok2005@163.com (G.Z.); 18511259982@163.com (Z.Y.); ajheqiuyue@163.com (Q.H.); ripplelj@126.com (J.L.); lipengjenny@126.com (P.L.); ychen0612@163.com (Y.C.); yaling110@163.com (X.Z.); sr1982@sdaeu.edu.cn (R.S.)
* Correspondence: wfz0814@126.com

Abstract: The construction of semiconductor heterojunction photocatalysts that improve the separation and transfer of photoinduced charge carriers is an effective and widely employed strategy to boost photocatalytic performance. Herein, we have successfully constructed a CdS/Ag/Bi_2WO_6 Z-scheme heterojunction with an Ag-bridge as an effective charge transfer channel by a facile process. The heterostructure consists of both CdS and Ag nanoparticles anchored on the surface of Bi_2WO_6 nanosheets. The photocatalytic efficiency of the CdS/Ag/Bi_2WO_6 system was studied by the decontamination of tetracycline (TC) and Rhodamine B (RhB) under visible light irradiation ($\lambda \geq 420$). The results exhibited that CdS/Ag/Bi_2WO_6 shows markedly higher photocatalytic performance than that of CdS, Bi_2WO_6, Ag/Bi_2WO_6, and CdS/Bi_2WO_6. The trapping experiment results verified that the $^{\bullet}O_2^-$ and h^+ radicals are the key active species. The results of photoluminescence spectral analysis and photocurrent responses indicated that the CdS/Ag/Bi_2WO_6 heterojunctions exhibit exceptional efficiency in separating and transferring photoinduced electron−hole pairs. Based on a series of characterization results, the boosted photocatalytic activity of the CdS/Ag/Bi_2WO_6 system is mostly due to the successful formation of the Ag-bridged Z-scheme heterojunction; these can not only inhibit the recombination rate of photoinduced charge carriers but also possess a splendid redox capacity. The work provides a way for designing a Z-scheme photocatalytic system based on Ag-bridged for boosting photocatalytic performance.

Keywords: Z-scheme; photocatalysis; CdS/Ag/Bi_2WO_6; Ag-bridged; visible light

Citation: Wang, F.; Jiang, L.; Zhang, G.; Ye, Z.; He, Q.; Li, J.; Li, P.; Chen, Y.; Zhou, X.; Shang, R. Novel Ag-Bridged Z-Scheme CdS/Ag/Bi_2WO_6 Heterojunction: Excellent Photocatalytic Performance and Insight into the Underlying Mechanism. *Nanomaterials* **2024**, *14*, 315. https://doi.org/10.3390/nano14030315

Academic Editors: Vincenzo Vaiano and Antonino Gulino

Received: 30 December 2023
Revised: 30 January 2024
Accepted: 2 February 2024
Published: 4 February 2024

1. Introduction

The rapid advancement of human society has led to an increasing focus on the issues of energy scarcity and environmental pollution. As a promising and eco-friendly technology that uses solar energy to address environmental problems and energy scarcity, semiconductor-based photocatalysis has recently received significant attention [1–4]. However, the traditional photocatalysts are only photoexcited in the ultraviolet, which only accounts for 4% of the total solar spectrum, thus considerably restraining their practical application [5,6]. Therefore, it is imperative to develop new visible-light-driven (VLD) photocatalysts [7].

Bismuth tungstate (Bi_2WO_6), a representative aurivillius oxide, possesses a unique layered structure composed of alternating $[WO_4]^{2-}$ octahedral layers and $[Bi_2O_2]^{2+}$ layers; this was advantageous for the transmission of photogenerated carriers. Bi_2WO_6 has a suitable band gap of approximately 2.7 eV, which has been regarded as a promising VLD photocatalyst [8,9]. In addition, Bi_2WO_6 possesses numerous advantages, such as chemical stability, nontoxicity, and corrosion resistance. However, the UV-to-visible

photo-absorption region of Bi_2WO_6 is shorter than approximately 450 nm. And swift recombination of photoinduced charge carriers extremely restricts its energy conversion efficiency [10,11]. To surmount these problems and improve the photocatalytic properties of pristine Bi_2WO_6, various techniques have been developed, such as morphological control [12,13], noble metal element doping [14,15], non-noble metal element doping [16,17], building heterojunction nanocomposite [18,19], and so on. Among these, the construction of heterostructures is a promising method, particularly the construction of Z-scheme photocatalytic systems [20,21]. The Z-scheme photocatalytic system can not only improve the transfer efficiency of photoexcited electrons and holes but also ensure a powerful redox capacity [22].

Among the connection modes of Z-scheme photocatalytic systems, ternary semiconductor/conductor/semiconductor Z-scheme heterojunctions in which two different semiconductors have a matching band structure can prominently enhance the photocatalytic performance [23,24]. Recently, noble metals (such as Ag, Pt, and Au) have been used as charge-carrying mediators, which can quickly transfer interfacial charge between two semiconductors. Besides, noble metal nanoparticles have a surface plasmon resonance during photocatalytic reactions. In recent years, various semiconductor/noble-metal/semiconductor Z-scheme heterojunctions, such as $CdS/Ag/g\text{-}C_3N_4$ [25], $g\text{-}C_3N_4@Ag/BiVO_4$ [26], $Co_3O_4/Ag/Bi_2WO_6$ [27], $CdS/Au/BiVO_4$ [28], $BaTiO_3/Au/g\text{-}C_3N_4$ [29], $g\text{-}C_3N_4/Ag/MoS_2$ [30], $g\text{-}C_3N_4/Pt/Bi_2WO_6$ [31], $BiVO_4/Au/CdS$ [32], $MoS_2/Au/g\text{-}C_3N_4$ [33], etc., have been successfully synthesized. Xiao et al. [34] constructed $C_3N_4@Ag\text{-}Bi_2WO_6$ by a facile process, and the ternary system showed a boosted photocatalytic capacity for degrading RhB and producing H_2 than that of single- and two-component systems; this was mainly due to the Z-scheme delivery mechanism. Gao et al. [35] successfully prepared $BiVO_4/Ag/CdS$ Z-scheme heterojunction, which attained improved ability in synergistic adsorption and photocatalytic degradation of fluoroquinolones. Hence, constructing a ternary semiconductor/noble metal/Bi_2WO_6 Z-scheme heterojunction could be a very promising strategy to obtain excellent photocatalytic activity.

Cadmium sulfide (CdS) is a narrow-bandgap semiconductor with a band gap of about 2.4 eV, which has been attracting much attention for environmental contaminant purification and hydrogen generation [36–38]. As a consequence, CdS is usually coupled with various photocatalysts to enhance visible light absorption performance and the separation ability of photoinduced charge carriers [39–41]. Besides, CdS is a very suitable semiconductor for assembling heterojunctions based on Bi_2WO_6, because the CB and VB of CdS are matched well with Bi_2WO_6 [42–44]. Zhang et al. [45] prepared Z-scheme CdS/Bi_2WO_6 heterojunction via a simple hydrothermal method, and they found that 15% CdS/Bi_2WO_6 photocatalysts could remove 60.82% of Cr(VI) and photodegrade almost all Rhodamine B within 1 h.

In this study, we design and synthesize ternary $CdS/Ag/Bi_2WO_6$ Z-scheme heterojunction by a facile process. The photocatalytic experiments exhibited that this ternary $CdS/Ag/Bi_2WO_6$ Z-scheme displayed excellent photocatalytic performances toward photodegrading Rhodamine B (RhB) and tetracycline (TC) under visible-light irradiation. The Ag nanoparticles can act as a charge transfer bridge between Bi_2WO_6 and CdS; this could boost the transfer rate of photoinduced electrons and holes in this Z-scheme system. Moreover, a plausible mechanism was investigated and proposed for explaining the excellent photocatalytic performance of $CdS/Ag/Bi_2WO_6$ heterojunctions.

2. Materials and Methods

2.1. Preparation of Bi_2WO_6

Bi_2WO_6 photocatalysts were synthesized via a simple hydrothermal method. Dissolve 2 mmol $Bi(NO_3)_3{\cdot}5H_2O$, 1 mmol $Na_2WO_4{\cdot}2H_2O$, and 0.05 g of cetyltrimethylammonium bromide (CTAB) in diluted nitric acid and vigorously stir for 30 min to acquire a uniform suspension. The pH of the aforementioned suspension was adjusted to approximately 7 by NaOH solutions. After stirring for 30 min, the resultant solution was poured into a

100 mL Teflon-lined stainless autoclave and heated at 180 °C for 24 h. The precipitate was subsequently filtered and washed with distilled water and ethanol several times, then dried at 80 °C for 8 h.

2.2. Preparation of Ag/Bi_2WO_6

The Ag/Bi_2WO_6 photocatalyst was prepared using a photo-reduction method. To be specific, a certain amount of $AgNO_3$ (0.05 mmol) was added to 50 mL of distilled water and then stirred until $AgNO_3$ was completely dissolved in the dark. Afterward, the as-synthetized Bi_2WO_6 (1 mmol) was added to the $AgNO_3$ solution and irradiated by 500 W Xe light (1 h) with vigorous stirring. Then the Ag/Bi_2WO_6 was collected and dried in a vacuum oven at 60 °C for 8 h.

2.3. Preparation of CdS/Ag/Bi_2WO_6

The CdS/Ag/Bi_2WO_6 was prepared using a precipitation method. A certain amount of $Cd(NO_3)_2 \cdot 4H_2O$ and 0.2 g of Ag/Bi_2WO_6 were dispersed in 30 mL of distilled water with ultrasonic vibration for 30 min. Subsequently, 20 mL of Na_2S solution was dropwise added to the above solution and stirred for 4 h. The precipitate was filtered and washed with distilled water and ethanol several times, and finally dried at 80 °C overnight. The mass ratio of CdS:Ag/Bi_2WO_6 was controlled to be 0.04. Similarly, CdS/Bi_2WO_6 were prepared under the same conditions.

2.4. Characterization of Photocatalysts

The phase structures of the prepared samples were measured by X-ray diffraction (XRD) (D/MAX-RB; Rigaku, Tokyo, Japan). The diffraction patterns were examined in the 2θ range from 20° to 80° with a Cu Kα source (λ = 0.15405) running at 40 kV and 30 mA. The morphology of the samples was examined by scanning electron microscopy (SEM; S-4800; Hitachi, Hitachi-shi, Japan). Transmission electron microscopy (TEM) and high-resolution TEM (HRTEM) images were analyzed with a transmission electron microscope (FEI Talos F200X G2, Thermo Scientific, Waltham, MA, USA) at an accelerating voltage of 200 kV. The UV–vis diffuse reflectance spectra (DRS) were collected via a UV–vis spectrophotometer (T9s; Persee, Beijing, China) equipped with an integrating sphere. Barium sulfate ($BaSO_4$) was used as the reference. Photoluminescence (PL) spectra data of the samples were recorded by a fluorescence spectrophotometer (F-4500; Hitachi, Japan).

2.5. Photocatalytic Experiments

The photocatalytic performances of the photocatalysts were assessed via the photodegradation of Rhodamine B (RhB) and tetracycline (TC) under visible light irradiation. A 400 W Xe lamp with a cut-off filter $\lambda \geq 420$ nm served as a light source. In each photocatalytic degradation test, 40 mg of the as-obtained photocatalyst was dispersed in 40 mL of 10 mg/L RhB solution (or 20 mg/L TC). Prior to light irradiation, the prepared suspensions were stirred in the dark for 1 h to reach adsorption-desorption equilibrium. The RhB and TC concentrations were recorded by a UV–vis spectrophotometer at 553 and 357 nm, respectively. The degradation performance was evaluated using the ratios (C/C_0) of the RhB and TC concentrations (C_0 was the initial concentration, and C was the concentration at a given time).

2.6. Photoelectrochemical Measurements

Photoelectrochemical measurements were performed on an electrochemical workstation (5060F; RST, Zhengzhou, China) in a conventional three-electrode system with a 0.5 M Na_2SO_4 aqueous solution. The samples, a saturated calomel electrode, and a Pt wire were used as the working, reference electrode, and counter electrodes, respectively. The light source was provided by a 100 W incandescent lamp with a 420 nm cut-off filter. The working electrode was manufactured as follows: 5 mg of photocatalyst was dispersed homogeneously in a certain amount of Nafion solution and ethanol (v/v = 30:1). Finally,

the as-prepared samples were loaded onto the bottom middle of ITO glass with a diameter of 6 mm. Then the photocurrents of the samples with the light on and off were measured at 0.8 V.

3. Results and Discussion

3.1. Crystal Structure Analysis

The crystal structures of Bi_2WO_6, Ag/Bi_2WO_6, CdS/Bi_2WO_6, $CdS/Ag/Bi_2WO_6$, and CdS were investigated using XRD. From Figure 1A, all diffraction peaks were completely corresponding to the structure of orthorhombic Bi_2WO_6 (JCPDS Card No. 39-0256). The characteristic peaks at 2θ = 28.3°, 32.8°, 47.1°, 55.8°, and 58.5° were attributed to the (1 3 1), (2 0 0), (2 0 2), (3 3 1), and (2 6 2) crystal planes, respectively. Comparing the curves of Bi_2WO_6 and Ag/Bi_2WO_6, it can be observed that they have similar patterns. This finding was consistent with the previous results [34]. This may be because of the low loading amount of Ag nanoparticles in the heterojunction. Furthermore, no characteristic diffraction peaks for CdS were observed in CdS/Bi_2WO_6 and $CdS/Ag/Bi_2WO_6$, which could be caused by the high dispersion, small particles, and small amount of CdS dopant. Similar results were found in CdS/Bi_2WO_6 [42] and CdS/BiOCl [46]. Figure 1B displays the XRD pattern of pure CdS, which can be assigned to the cubic phase of CdS (JCPDS Card No. 89-0440) [47]. The diffraction peaks at 26.4°, 43.9°, and 51.9° were well-matched with the crystal planes of (1 1 1), (2 2 0), and (3 1 1) of CdS, respectively. The existence of Ag nanoparticles and/or CdS in $CdS/Ag/Bi_2WO_6$ composites was further identified by TEM analysis.

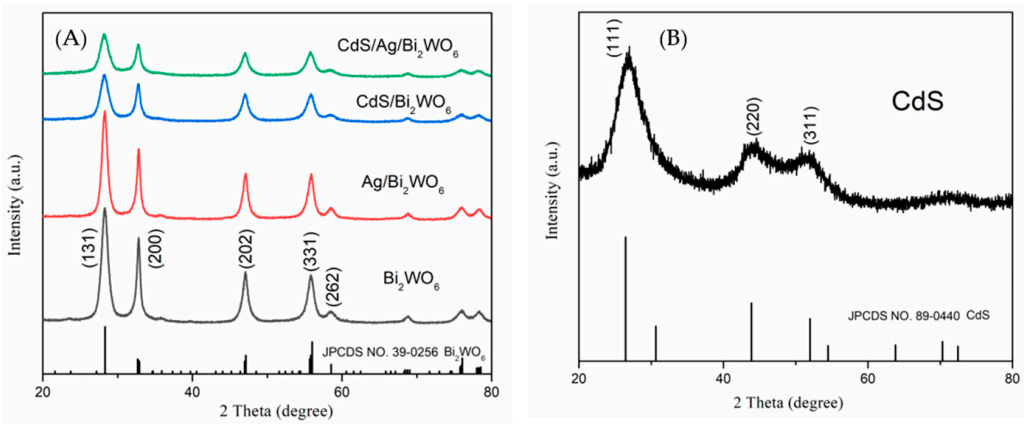

Figure 1. XRD patterns of Bi_2WO_6, Ag/Bi_2WO_6, CdS/Bi_2WO_6, $CdS/Ag/Bi_2WO_6$ (**A**), and CdS (**B**).

3.2. Morphology Characterization

The morphologies of Bi_2WO_6, Ag/Bi_2WO_6, CdS/Bi_2WO_6, and $CdS/Ag/Bi_2WO_6$ composites were studied by scanning electron microscope (SEM; S-4800; Hitachi, Hitachi-shi, Japan). As could be observed from Figure 2A, the Bi_2WO_6 showed an aggregated nanosheet-like microstructure. It was worth noting that Ag nanoparticles on the surface of Bi_2WO_6 were found, indicating that Ag nanoparticles were successfully deposited on the Bi_2WO_6 surface (Figure 2B). The SEM images of CdS/Bi_2WO_6 and $CdS/Ag/Bi_2WO_6$ composites (Figure 2C,D) were found to be similar to pure Bi_2WO_6. This similarity could be attributed to the use of the same original Bi_2WO_6 material, as well as high dispersion and the small particle size of CdS in the composites.

The morphologies of the $CdS/Ag/Bi_2WO_6$ were further observed by transmission electron microscopy (TEM) and high-resolution transmission electron microscopy (HRTEM). From Figure 3A,B, the $CdS/Ag/Bi_2WO_6$ sample showed an irregular and nanosheet-like microstructure. The HRTEM image (Figure 3C) displays that some nanoparticles have grown on the Bi_2WO_6 nanosheet. It is worth noting that the edges of Bi_2WO_6 nanosheets appear to have two different types of nanoparticles, which may be Ag and CdS nanoparticles. The HRTEM image (Figure 3D) shows the crystal plane spacing of 0.23,

0.34, and 0.27 nm; these correspond to the (1 1 1) plane of Ag nanoparticles, the (1 1 1) plane of CdS, and the (2 0 0) plane of Bi_2WO_6, respectively. Furthermore, Ag nanoparticles loaded on Bi_2WO_6 nanosheets are in close contact with CdS. It shows that CdS and Ag nanoparticles were successfully supported on the Bi_2WO_6 nanosheet, which could be beneficial for charge separation within the Z-scheme CdS/Ag/Bi_2WO_6 heterojunctions in comparison to pure Bi_2WO_6. Moreover, the elemental mapping method was employed to investigate the composition distribution in CdS/Ag/Bi_2WO_6 samples. As depicted in Figure 3E1–E6, W, O, Bi, Ag, Cd, and S elements are evenly distributed throughout the CdS/Ag/Bi_2WO_6 sample. And the element mapping distribution of Ag, Cd, and S proved evidence that CdS, Ag, and Bi_2WO_6 are closely combined. Combined with the TEM results, it can be indicated that CdS and Ag nanoparticles were evenly loaded on the surface of Bi_2WO_6 nanosheets.

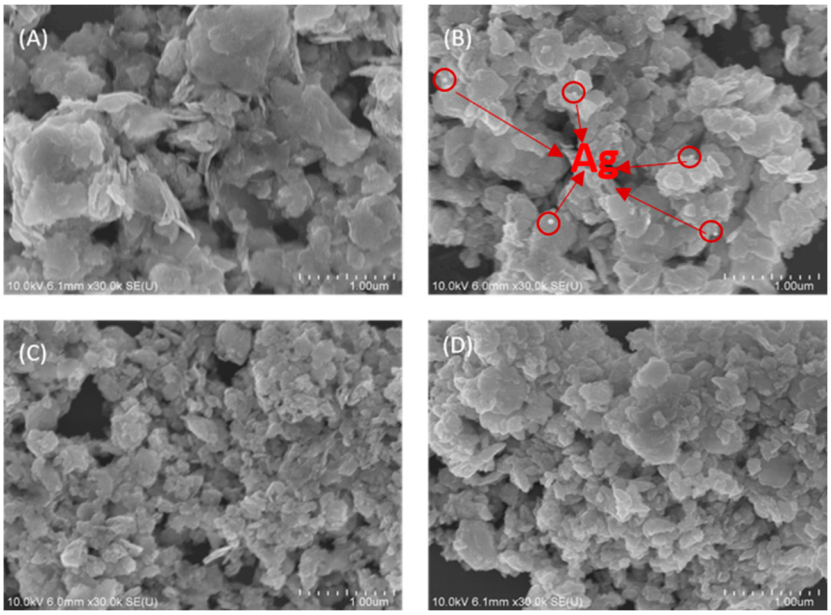

Figure 2. SEM images of (**A**) Bi_2WO_6, (**B**) Ag/Bi_2WO_6, (**C**) CdS/Bi_2WO_6, and (**D**) CdS/Ag/Bi_2WO_6.

3.3. Optical Properties

The light absorption properties of the obtained samples were characterized by UV–vis DRS, as illustrated in Figure 4. The absorption edges were observed at approximately 450 nm and 650 nm for Bi_2WO_6 and CdS, respectively. The optical absorption edge of the CdS/Bi_2WO_6 composite was distinctly red-shifted compared with Bi_2WO_6, which could be assigned to the forming heterojunction between CdS and Bi_2WO_6. Meanwhile, after Ag nanoparticles growth on the surface of Bi_2WO_6 nanosheets, Ag/Bi_2WO_6 had a wide absorption in the visible light region; this may be attributed to the surface plasmon resonance effect of spatially confined electrons in Ag nanoparticles [48]. Compared with all other samples, the obtained CdS/Ag/Bi_2WO_6 ternary system exhibited enhanced visible light absorption, which may be on account of the synergetic effect of CdS and Ag. These results reveal that the as-prepared CdS/Ag/Bi_2WO_6 heterojunction photocatalyst had an excellent visible-light absorption range and thus produced more photoinduced electron−hole pairs, as demonstrated subsequently. The Kubelka-Munk formula: $ahv = A(hv - Eg)^{n/2}$ was used to estimate the band gap values of CdS and Bi_2WO_6 [49]. For CdS and Bi_2WO_6, the values of n are 1 and 4, respectively [50,51]. From the inset of Figure 4, the band gap values of CdS and Bi_2WO_6 are approximately 2.17 eV and 2.81 eV, respectively.

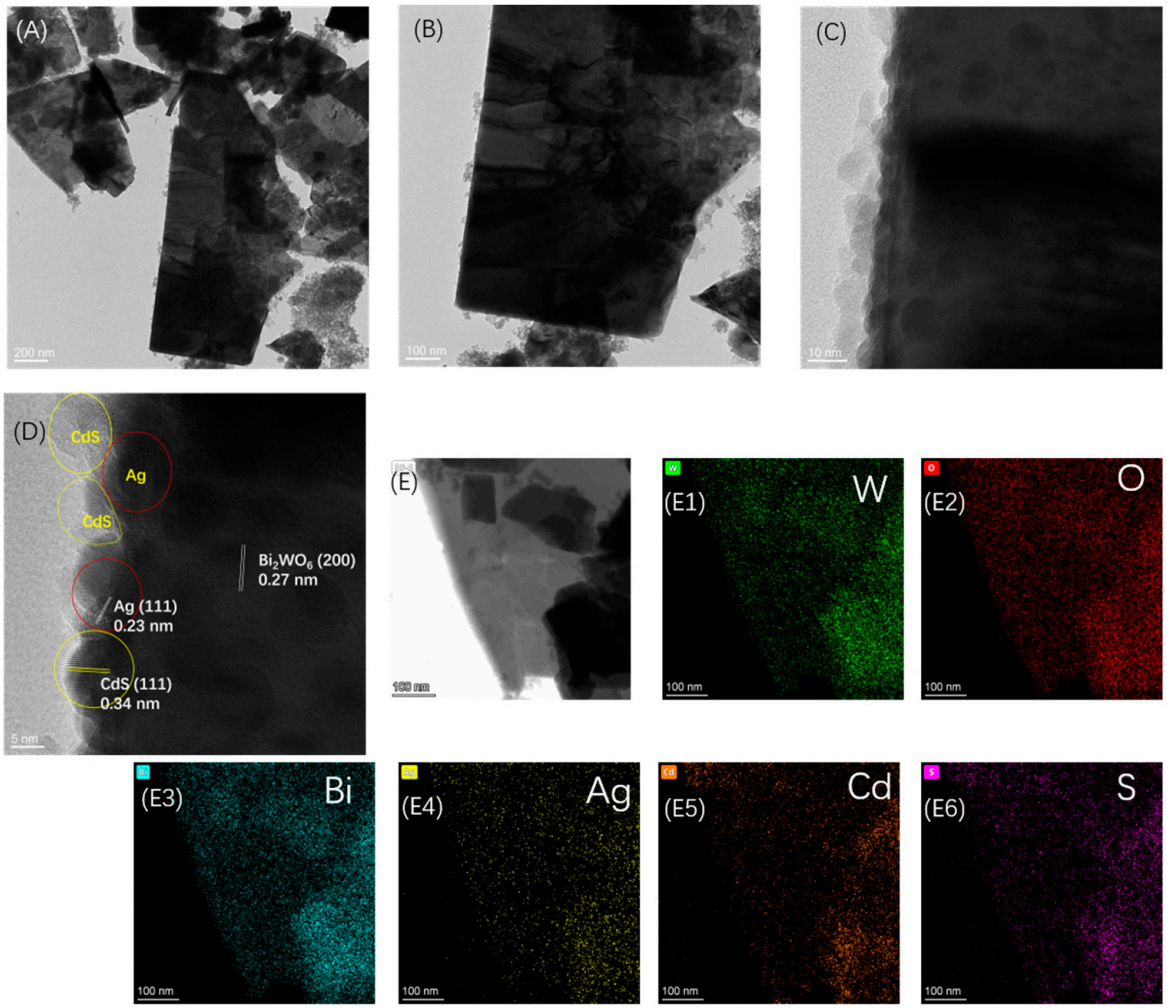

Figure 3. TEM images (**A**,**B**) and HRTEM images (**C**,**D**) of CdS/Ag/Bi_2WO_6; (**E**,**E1**–**E6**) the elemental mapping of W, O, Bi, Ag, Cd, and S of CdS/Ag/Bi_2WO_6.

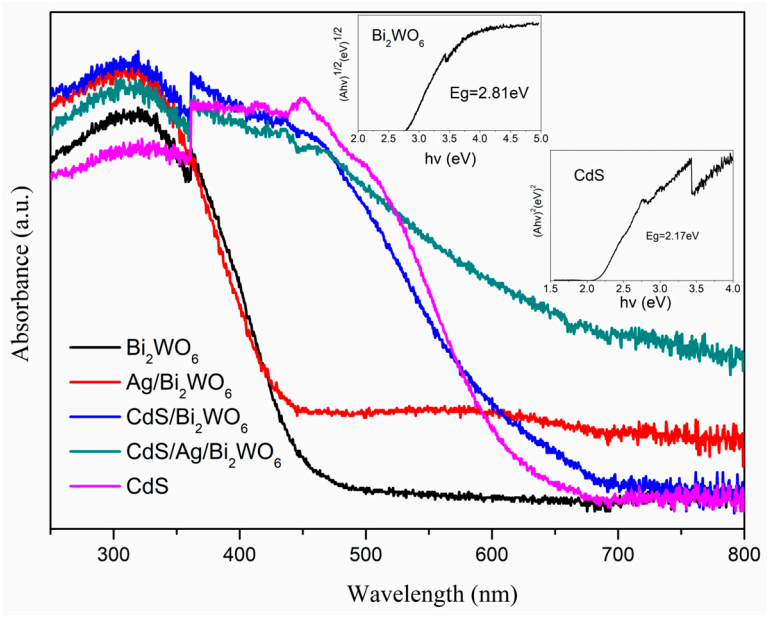

Figure 4. DRS spectra of pure Bi_2WO_6, Ag/Bi_2WO_6, CdS/Bi_2WO_6, and CdS/Ag/Bi_2WO_6; the inset shows the band gap energies of CdS and Bi_2WO_6.

3.4. Photocatalytic Performances of the Samples

The photocatalytic performance of pure CdS, Bi_2WO_6, Ag/Bi_2WO_6, CdS/Bi_2WO_6, and $CdS/Ag/Bi_2WO_6$ was assessed via monitoring the photodegradation of RhB under visible light illumination ($\lambda \geq 420$ nm). All catalysts were dispersed in RhB solution and then magnetically stirred in a dark environment for 60 min to attain an adsorption–desorption equilibrium. The adsorption capacity of all photocatalysts for RhB is shown in Figure 5A. The results indicated that the pure Bi_2WO_6 photocatalyst exhibits the highest adsorption capacity among all the photocatalysts, while the pure CdS photocatalyst has the lowest adsorption capacity. Additionally, Ag/Bi_2WO_6, CdS/Bi_2WO_6, and $CdS/Ag/Bi_2WO_6$ samples demonstrate similar capacities for RhB adsorption. From Figure 5B, it was found that the RhB degradation efficiencies over the Bi_2WO_6, CdS, Ag/Bi_2WO_6, CdS/Bi_2WO_6, and $CdS/Ag/Bi_2WO_6$ under visible light illumination for 40 min are about 45.8%, 53.2%, 82.2%, 90.5%, and 98.6%, respectively. Obviously, of all the as-prepared photocatalysts, Z-scheme $CdS/Ag/Bi_2WO_6$ heterojunction exhibited the greatest photocatalytic degradation effect, which was 2.15 and 1.85 times higher than the pure Bi_2WO_6 and CdS, respectively. The superior photocatalytic activity of $CdS/Ag/Bi_2WO_6$ could be because this Z-scheme ternary system has a stronger absorption capacity for visible light and excellent separation and transmission of photoinduced carriers compared to other photocatalysts.

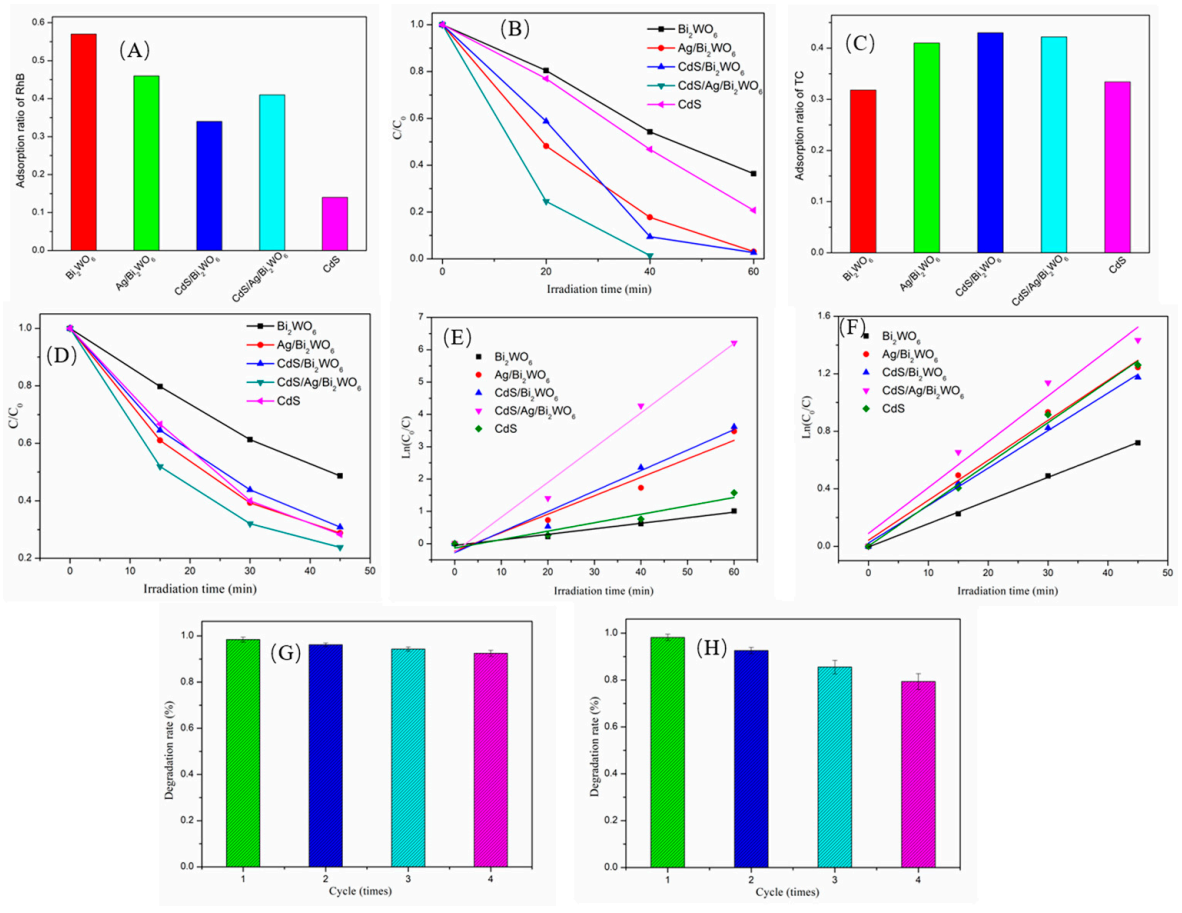

Figure 5. Adsorption ratio of RhB (**A**) and TC (**C**) in the dark; photodegradation of RhB (**B**) and TC (**D**) with different photocatalysts under visible light irradiation ($\lambda \geq 420$ nm); the pseudo-first-order reaction kinetics of the RhB (**E**) and TC (**F**) degradation over different photocatalysts; cyclic photodegradation of RhB by $CdS/Ag/Bi_2WO_6$ photocatalyst with (**G**) and without (**H**) the regeneration procedure.

In addition to RhB, other colorless pollutants, such as Tetracycline (TC), were also selected to estimate the photocatalytic efficiency of Bi_2WO_6, CdS, Ag/Bi_2WO_6, CdS/Bi_2WO_6,

and CdS/Ag/Bi_2WO_6 under visible-light illumination ($\lambda \geq 420$ nm). Before irradiation, the adsorption capacities of Bi_2WO_6, CdS, Ag/Bi_2WO_6, CdS/Bi_2WO_6, and CdS/Ag/Bi_2WO_6 were also subjected to 60 min in a dark environment. As depicted in Figure 5C, the adsorption ratios of Bi_2WO_6, CdS, Ag/Bi_2WO_6, CdS/Bi_2WO_6, and CdS/Ag/Bi_2WO_6 are approximately 0.318, 0.330, 0.410, 0.430, and 0.422, respectively. Unlike the adsorption of RhB, Ag/Bi_2WO_6, CdS/Bi_2WO_6, and CdS/Ag/Bi_2WO_6 have a higher adsorption capacity for TC. From Figure 5D, after the adsorption–desorption equilibrium, it can be discovered that the Z-scheme CdS/Ag/Bi_2WO_6 heterojunction presented the optimal photocatalytic activity, with a TC photodegradation efficiency of about 78% after 45 min of visible light illumination.

The kinetic behavior of the Bi_2WO_6, CdS, Ag/Bi_2WO_6, CdS/Bi_2WO_6, and CdS/Ag/Bi_2WO_6 photocatalysts in the RhB and TC degradation processes is displayed in Figures 5E and 5F, respectively. Moreover, the pseudo-first-order equation was employed to fit the kinetic process. The $Ln(C/C_0) \sim$ reaction time (t) curves exhibited linear variations, indicating that the photocatalytic degradation data of RhB and TC followed the first-level reaction kinetics law. The rate constants (RhB) of Bi_2WO_6, CdS, Ag/Bi_2WO_6, CdS/Bi_2WO_6, and CdS/Ag/Bi_2WO_6 were calculated as 0.0171, 0.0261, 0.0571, 0.0634, and 0.1075 min^{-1}, respectively. Similarly, the rate constants (TC) of the Bi_2WO_6, CdS, Ag/Bi_2WO_6, CdS/Bi_2WO_6, and CdS/Ag/Bi_2WO_6 were determined as 0.0161, 0.0286, 0.0278, 0.0261, and 0.0319 min^{-1}, respectively. It was evident that, compared with single- and two-component photocatalysts, the reaction rate of CdS/Ag/Bi_2WO_6 heterojunction has been significantly improved.

From the perspective of future practical applications, the repeatability and stability of the catalysts play a crucial role. Therefore, to evaluate the repeatability and stability of the CdS/Ag/Bi_2WO_6, recycling experiments were conducted using the heterojunction photocatalyst for RhB photodegradation (Figure 5G). The recovery process of the photocatalyst is as follows: after each degradation cycle, collect the photocatalyst powder, wash it three times with distilled water and ethanol, dry it, and proceed with subsequent photocatalysis. In the cyclic experiment, the error bars were derived from three batches of CdS/Ag/Bi_2WO_6 samples, representing the standard deviation. It can be observed that CdS/Ag/Bi_2WO_6 maintains high degradation efficiency after four cycles. As a comparison, in the cyclic experiment, no regeneration treatment was applied to directly use the collected photocatalyst powder. The results are shown in Figure 5H. After four cyclic experiments, there is a slight decrease in photocatalytic degradation efficiency compared to previous regeneration procedures. This may be attributed to pollutants adsorption on its surface after the experiment, which reduces active site availability and performance deterioration. This finding indicated remarkable stability of the Z-scheme CdS/Ag/Bi_2WO_6 heterojunction.

3.5. Photocatalytic Mechanism of CdS/Ag/Bi_2WO_6 Heterojunction Photocatalyst

Trapping experiments were performed to identify the key reactive radicals and further understand the probable catalytic mechanism. In the CdS/Ag/Bi_2WO_6 photocatalytic reaction system, isopropanol (IPA, 10 mM), sodium oxalate ($Na_2C_2O_4$, 10 mM), and benzoquinone (BQ, 1 mM) were used as scavengers of hydroxyl radicals ($^{\bullet}OH$), holes (h^+), and superoxide ions ($^{\bullet}O_2^-$), respectively. As displayed in Figure 6, the degradation efficiency of CdS/Ag/Bi_2WO_6 was slightly inhibited when IPA was added, implying that $^{\bullet}OH$ may not play a main role in the photodegradation of RhB. After adding BQ or $Na_2C_2O_4$, the degradation performance of the CdS/Ag/Bi_2WO_6 photocatalyst was dramatically inhibited, which confirmed that $^{\bullet}O_2^-$ and h^+ were the key active species in the CdS/Ag/Bi_2WO_6 photocatalytic reaction.

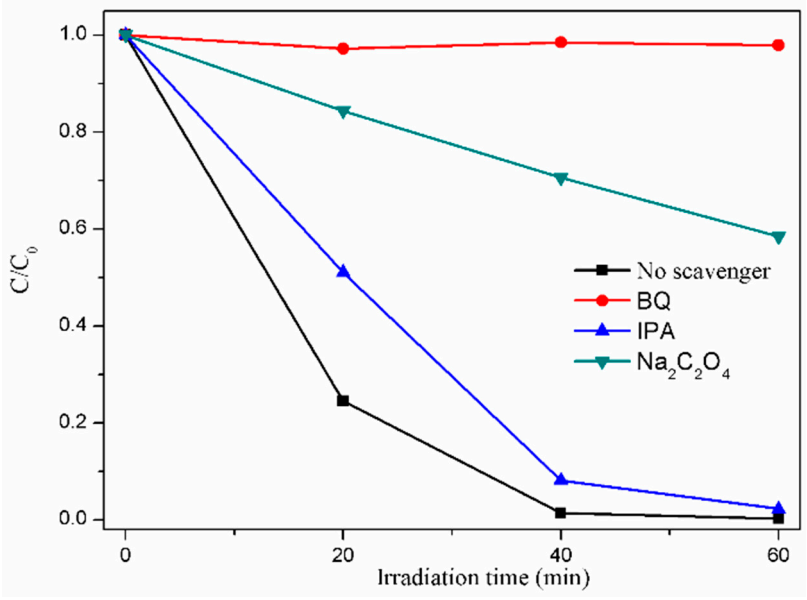

Figure 6. The species trapping experiments of CdS/Ag/Bi_2WO_6 under visible light irradiation.

The recombination efficiency of photoinduced electron-hole pairs was analyzed using photoluminescence (PL) spectroscopy. The weaker PL intensity typically indicates a lower possibility of photoinduced electron-hole recombination [52]. From Figure 7, the PL spectra of pure Bi_2WO_6, Ag/Bi_2WO_6, CdS/Bi_2WO_6, and CdS/Ag/Bi_2WO_6 are in the range of 350–700 nm, and all intense emission peaks are at about 468 nm. It is observed that the order of the emission intensity of the catalysts is: Bi_2WO_6 > Ag/Bi_2WO_6 > CdS/Bi_2WO_6 > CdS/Ag/Bi_2WO_6. The results confirmed that the CdS/Ag/Bi_2WO_6 heterojunctions possess the strongest separation efficiency of photoinduced charge carriers, suggesting they have superior photocatalytic performance.

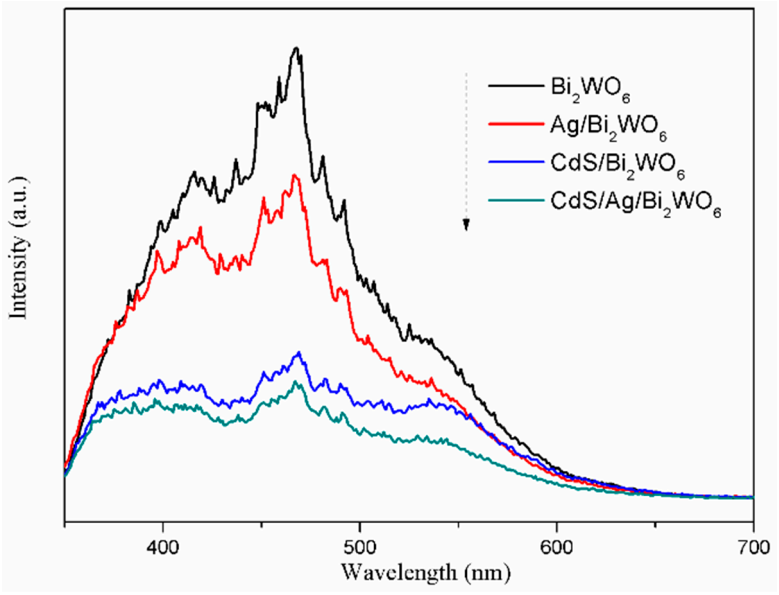

Figure 7. Photoluminescence spectra of Bi_2WO_6, Ag/Bi_2WO_6, CdS/Bi_2WO_6, and CdS/Ag/Bi_2WO_6.

To further recognize the transmission and separation of photogenerated charge in CdS/Ag/Bi_2WO_6, the photocurrent response measurement is also employed under visible light irradiation. The higher photocurrent intensity means that the transmission efficiency of photogenerated carriers is higher, which results in outstanding photocatalytic activity [53]. Figure 8 shows the regular photocurrent responses of pure Bi_2WO_6, Ag/Bi_2WO_6,

CdS/Bi_2WO_6, and $CdS/Ag/Bi_2WO_6$ in the dark and light. The photocurrent density increases in the order Bi_2WO_6, Ag/Bi_2WO_6, CdS/Bi_2WO_6, and $CdS/Ag/Bi_2WO_6$, which corresponds with their PL and photocatalytic properties. Therefore, given the above results, the as-prepared $CdS/Ag/Bi_2WO_6$ ternary heterojunction system can considerably enhance photogenerated charge transfer and separation efficiency, thereby improving photocatalytic performance.

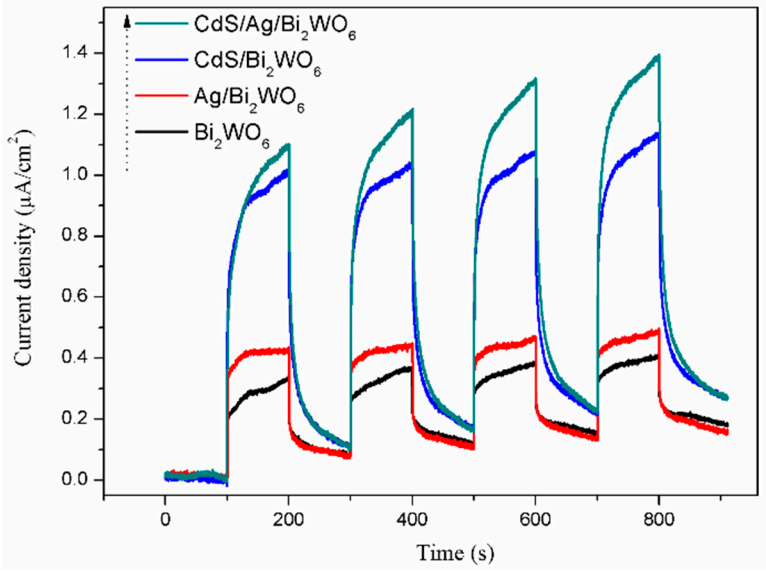

Figure 8. Photocurent responses of pure Bi_2WO_6, Ag/Bi_2WO_6, CdS/Bi_2WO_6, and $CdS/Ag/Bi_2WO_6$.

To systematically explore the photocatalytic mechanism, it is necessary to calculate the position of the conduction band (CB) and valence band (VB) using the following equation:

$$E_{VB} = \chi - E_e + 0.5E_g \quad (1)$$

$$E_{CB} = E_{VB} - E_g \quad (2)$$

χ value is the Mulliken electronegativity of Bi_2WO_6 (6.39 eV [54]) and CdS (5.18 eV [55]). The band gap values of Bi_2WO_6 and CdS were 2.81 and 2.17 eV, respectively. The calculated E_{VB} values of Bi_2WO_6 and CdS were 3.29 and 1.76 eV, respectively, and their corresponding E_{CB} values were 0.48 and −0.41 eV. With the determination of the CB and VB values of Bi_2WO_6 and CdS, the transport itinerary of photoinduced electron−hole pairs gradually becomes clear.

According to the charge carrier transfer mode of a typical type-II heterostructure, the photogenerated electrons on the CB of CdS will migrate to the CB of Bi_2WO_6. Because the conduction band of potential Bi_2WO_6 is more positive than the $E(O_2/{}^{\bullet}O_2^-)$ (−0.33 eV) [45], electrons on its CB cannot reduce O_2 into ${}^{\bullet}O_2^-$. However, from the results of trapping experiments, ${}^{\bullet}O_2^-$ was the key active species in the $CdS/Ag/Bi_2WO_6$ photocatalytic reaction system. This means that the $CdS/Ag/Bi_2WO_6$ system has a different photoinduced electron and hole transport itinerary from the Bi_2WO_6/CdS system, which may be derived from the formation of the Z-scheme system with Ag-bridge as an efficient charge transfer medium.

Based on the analysis of the above result, a plausible mechanism for illustrating the transport path of photogenerated electron−hole pairs over the $CdS/Ag/Bi_2WO_6$ heterojunctions was proposed, as presented schematically in Figure 9. Upon exposure of the $CdS/Ag/Bi_2WO_6$ photocatalyst to visible light, both Bi_2WO_6 and CdS can be excited and then generate photogenerated electrons and holes. Because the CB position of Bi_2WO_6 is more negative than the Fermi level of silver nanoparticles, electrons on its CB will be injected into the silver nanoparticles through the Schottky barrier. Meanwhile, the holes on the VB of CdS will transfer to silver nanoparticles. Therefore, electrons generated from the

CB of Bi_2WO_6 and holes generated from the VB of CdS can directly annihilate through the Ag nanoparticle bridge. The strong reductive electrons on the CB of CdS can react with dissolved oxygen molecules to form the active species $^{\bullet}O_2^-$, which can oxidize organic contaminants into decomposed products. And the holes on the VB of Bi_2WO_6 oxidize organic contaminants directly.

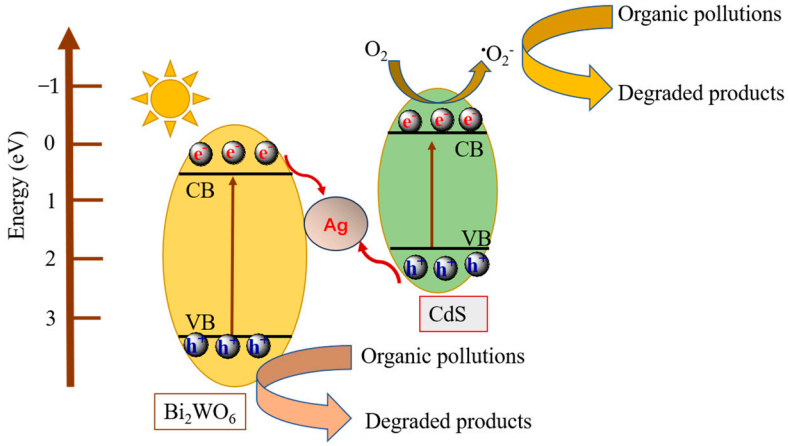

Figure 9. Schematic diagram of the proposed photogenerated charge separation and transmission over the CdS/Ag/Bi_2WO_6 heterojunctions under visible light irradiation.

The Z-scheme with Ag-bridge in the CdS/Ag/Bi_2WO_6 ternary system not only promotes the spatial isolation of the photoinduced electron−hole pairs but also can maintain powerful redox capability, thus significantly boosting the quantum yield and photocatalytic activity.

4. Conclusions

In summary, the CdS/Ag/Bi_2WO_6 Z-scheme heterojunction photocatalysts were successfully synthesized by hydrothermal, photoreduction, and precipitation methods. Compared with single- and two-component systems such as CdS, Bi_2WO_6, Ag/Bi_2WO_6, and CdS/Bi_2WO_6 samples, the CdS/Ag/Bi_2WO_6 Z-scheme heterojunction exhibited remarkably boosted photocatalytic performance for the degradation of RhB and TC under visible light irradiation ($\lambda \geq 420$ nm). The plausible photocatalytic mechanism was raised to explain the superior photocatalytic performance based on DRS and PL analysis, photocurrent responses, band edge positions, and the active species trapping experiment. In the CdS/Ag/Bi_2WO_6 Z-scheme heterojunctions system, the introduced Ag nanoparticles can be used as a bridge for the transportation of photogenerated charge carriers between CdS and Bi_2WO_6, thus accelerating photogenerated charge carrier separation and enhancing redox capacity. This work provided an effective method for the design and construction of extremely efficient photocatalysts based on semiconductor/noble-metal/semiconductor Z-scheme heterojunction composites.

Author Contributions: Conceptualization, F.W., L.J. and G.Z.; methodology, Z.Y. and F.W.; validation, Q.H. and J.L.; formal analysis, P.L. and G.Z.; investigation, Y.C. and L.J.; data curation, X.Z. and R.S.; writing—original draft preparation, F.W.; writing—review and editing, F.W. All authors have read and agreed to the published version of the manuscript.

Funding: This research was funded by the Natural Science Foundation of Shandong Province (ZR2022QB136), Shandong Key Research and Development Program (2022SFGC0302, 2023RKY06020), Central Guiding Local Science and Technology Development Special Project (YDZX2022152, YDZX2023013).

Data Availability Statement: The data presented in the study are available from the corresponding author.

Conflicts of Interest: The authors declare no conflict of interest.

References

1. Zhang, J.; Mück-Lichtenfeld, C.; Studer, A. Photocatalytic phosphine-mediated water activation for radical hydrogenation. *Nature* **2023**, *619*, 506–513. [CrossRef]
2. Bie, C.; Yu, H.; Cheng, B.; Ho, W.; Fan, J.; Yu, J. Design, fabrication, and mechanism of nitrogen-doped graphene-based photocatalyst. *Adv. Mater.* **2021**, *33*, 2003521. [CrossRef] [PubMed]
3. Ma, R.; Xue, Y.; Ma, Q.; Chen, Y.; Yuan, S.; Fan, J. Recent Advances in Carbon-Based Materials for Adsorptive and Photocatalytic Antibiotic Removal. *Nanomaterials* **2022**, *12*, 4045. [CrossRef] [PubMed]
4. Poudel, M.B.; Logeshwaran, N.; Kim, A.R.; Karthikeyan, S.C.; Subramanian, V.; Dong, J.Y. Integrated core-shell assembly of Ni_3S_2 nanowires and CoMoP nanosheets as highly efficient bifunctional electrocatalysts for overall water splitting. *J. Alloys Compd.* **2023**, *960*, 170678. [CrossRef]
5. Sanakousar, F.M.; Vidyasagar, C.C.; Jiménez-Pérez, V.M.; Prakash, K. Recent progress on visible-light-driven metal and non-metal doped ZnO nanostructures for photocatalytic degradation of organic pollutants. *Mat. Sci. Semicon. Proc.* **2022**, *140*, 106390. [CrossRef]
6. Qi, Y.; Zhao, S.; Jiang, X.; Kang, Z.; Gao, S.; Liu, W.; Shen, Y. Visible-Light-Driven BiOBr-TiO_2-Attapulgite Photocatalyst with Excellent Photocatalytic Activity for Multiple Xanthates. *Catalysts* **2023**, *13*, 1504. [CrossRef]
7. Poudel, M.B.; Yu, C.; Kim, H.J. Synthesis of conducting bifunctional polyaniline@Mn-TiO_2 nanocomposites for supercapacitor electrode and visible light driven photocatalysis. *Catalysts* **2020**, *10*, 546. [CrossRef]
8. Wang, F.; Li, W.; Gu, S.; Li, H.; Wu, W.; Liu, X. Samarium and nitrogen Co-doped Bi_2WO_6 photocatalysts: Synergistic effect of Sm^{3+}/Sm^{2+} redox centers and N-doped level for enhancing visible-light photocatalytic activity. *Chem. Eur. J.* **2016**, *22*, 12859–12867. [CrossRef] [PubMed]
9. He, Y.; Gao, H.; Liu, J. A Visible-Light-Active CuS/MoS_2/Bi_2WO_6 Aptamer Sensitively Detects the Non-Steroidal Anti-Inflammatory Drug Diclofenac. *Nanomaterials* **2022**, *12*, 2834. [CrossRef]
10. Liu, X.; Gu, S.; Zhao, Y.; Zhou, G.; Li, W. $BiVO_4$, Bi_2WO_6 and Bi_2MoO_6 photocatalysis: A brief review. *J. Mater. Sci. Technol.* **2020**, *56*, 45–68. [CrossRef]
11. Chen, T.; Liu, L.; Hu, C.; Huang, H. Recent advances on Bi_2WO_6-based photocatalysts for environmental and energy applications. *Chin. J. Catal.* **2021**, *42*, 1413–1438. [CrossRef]
12. Shang, Y.; Cui, Y.; Shi, R.; Yang, P. Effect of acetic acid on morphology of Bi_2WO_6 with enhanced photocatalytic activity. *Mat. Sci. Semicon. Proc.* **2019**, *89*, 240–249. [CrossRef]
13. Campos, W.E.O.; Nobre, F.X.; da Rocha Filho, G.N.; da Silva, M.A.R.; da Costa, C.E.F.; do Nascimento, L.A.S.; Zamian, J.R. High Photocatalytic Activity under Visible Light for a New Morphology of Bi_2WO_6 Microcrystals. *Catalysts* **2019**, *9*, 667. [CrossRef]
14. Chang, C.; Chen, J.; Lin, K.; Wei, Y.; Chao, P.; Huang, C. Enhanced visible-light-driven photocatalytic degradation by metal wire-mesh supported Ag/flower-like Bi_2WO_6 photocatalysts. *J. Alloys Compd.* **2020**, *813*, 152186. [CrossRef]
15. Pinchujit, S.; Phuruangrat, A.; Wannapop, S.; Sakhon, T.; Kuntalue, B.; Thongtem, T.; Thongtem, S. Synthesis and characterization of heterostructure Pt/Bi_2WO_6 nanocomposites with enhanced photodegradation efficiency induced by visible radiation. *Solid State Sci.* **2022**, *134*, 107064. [CrossRef]
16. Zhang, Y.; Zhao, Y.; Xiong, Z.; Gao, T.; Gong, B.; Liu, P.; Liu, J.; Zhang, J. Elemental mercury removal by I^--doped Bi_2WO_6 with remarkable visible-light-driven photocatalytic oxidation. *Appl. Catal. B* **2021**, *282*, 119534. [CrossRef]
17. Zhang, Y.; Yu, H.; Zhai, R.; Zhang, J.; Gao, C.; Qi, K.; Yang, L.; Ma, Q. Recent Progress in Photocatalytic Degradation of Water Pollution by Bismuth Tungstate. *Molecules* **2023**, *28*, 8011. [CrossRef]
18. Kovalevskiy, N.; Cherepanova, S.; Gerasimov, E.; Lyulyukin, M.; Solovyeva, M.; Prosvirin, I.; Kozlov, D.; Selishchev, D. Enhanced Photocatalytic Activity and Stability of Bi_2WO_6-TiO_2-N Nanocomposites in the Oxidation of Volatile Pollutants. *Nanomaterials* **2022**, *12*, 359. [CrossRef] [PubMed]
19. Wang, F.; Li, W.; Gu, S.; Li, H.; Wu, X.; Ren, C.; Liu, X. Facile fabrication of direct Z-scheme MoS_2/Bi_2WO_6 heterojunction photocatalyst with superior photocatalytic performance under visible light irradiation. *J. Photoch. Photobio. A* **2017**, *335*, 140–148. [CrossRef]
20. Qian, X.; Ma, Y.; Arif, M.; Xia, J.; He, G.; Chen, H. Construction of 2D/2D $Bi_4O_5Br_2$/Bi_2WO_6 Z-scheme heterojunction for highly efficient photodegradation of ciprofloxacin under visible light. *Sep. Purif. Technol.* **2023**, *316*, 123794. [CrossRef]
21. Zhou, P.; Yu, J.; Jaroniec, M. All-solid-state Z-scheme photocatalytic systems. *Adv. Mater.* **2014**, *26*, 4920–4935. [CrossRef]
22. Chen, Y.; Li, R.; Yang, L.; Wang, R.; Li, Z.; Li, T.; Liu, M.; Ramakrishna, S.; Long, Y. Synergistic Effects of Magnetic Z-Scheme g-C_3N_4/$CoFe_2O_4$ Nanofibres with Controllable Morphology on Photocatalytic Activity. *Nanomaterials* **2023**, *13*, 1142. [CrossRef]
23. Feng, S.; Chen, T.; Liu, Z.; Shi, J.; Yue, X.; Li, Y. Z-scheme CdS/CQDs/g-C_3N_4 composites with visible-near-infrared light response for efficient photocatalytic organic pollutant degradation. *Sci. Total Environ.* **2020**, *704*, 135404. [CrossRef]
24. Sun, Y.; Zhu, Q.; Bai, B.; Li, Y.; He, C. Novel all-solid-state Z-scheme SnO_2/Pt/In_2O_3 photocatalyst with boosted photocatalytic performance on water splitting and 2, 4-dichlorophenol degradation under visible light. *Chem. Eng. J.* **2020**, *390*, 124518. [CrossRef]

25. Qian, L.; Hou, Y.; Yu, Z.; Li, M.; Li, F.; Sun, L.; Luo, W.; Pan, G. Metal-induced Z-scheme CdS/Ag/g-C_3N_4 photocatalyst for enhanced hydrogen evolution under visible light: The synergy of MIP effect and electron mediator of Ag. *Mol. Catal.* **2018**, *458*, 43–51. [CrossRef]
26. Ou, M.; Wan, S.; Zhong, Q.; Zhang, S.; Song, Y.; Guo, L.; Cai, W.; Xu, Y. Hierarchical Z-scheme photocatalyst of g-C_3N_4@Ag/$BiVO_4$(040) with enhanced visible-light-induced photocatalytic oxidation performance. *Appl. Catal. B* **2018**, *221*, 97–107. [CrossRef]
27. Wan, J.; Xue, P.; Wang, R.; Liu, L.; Liu, E.; Bai, X.; Fan, J.; Hu, X. Synergistic effects in simultaneous photocatalytic removal of Cr (VI) and tetracycline hydrochloride by Z-scheme Co_3O_4/Ag/Bi_2WO_6 heterojunction. *Appl. Surf. Sci.* **2019**, *483*, 677–687. [CrossRef]
28. Bao, S.; Wu, Q.; Chang, S.; Tian, B.; Zhang, Z. Z-scheme CdS–Au–$BiVO_4$ with enhanced photocatalytic activity for organic contaminant decomposition. *Catal. Sci. Technol.* **2017**, *7*, 124–132. [CrossRef]
29. Wu, M.; Ding, T.; Wang, Y.; Zhao, W.; Xian, H.; Tian, Y.; Zhang, T.; Li, X. Rational construction of plasmon Au assisted ferroelectric-$BaTiO_3$/Au/g-C_3N_4 Z-scheme system for efficient photocatalysis. *Catal. Today* **2020**, *355*, 311–318. [CrossRef]
30. Lu, D.; Wang, H.; Zhao, X.; Kondamareddy, K.K.; Ding, J.; Li, C.; Fang, P. Highly efficient visible-light-induced photoactivity of Z-scheme g-C_3N_4/Ag/MoS_2 ternary photocatalysts for organic pollutant degradation and production of hydrogen. *ACS Sustain. Chem. Eng.* **2017**, *5*, 1436–1445. [CrossRef]
31. Zhang, Y.; Chai, C.; Zhang, X.; Liu, J.; Duan, D.; Fan, C.; Wang, Y. Construction of Pt-decorated g-C_3N_4/Bi_2WO_6 Z-scheme composite with superior solar photocatalytic activity toward rhodamine B degradation. *Inorg. Chem. Commun.* **2019**, *100*, 81–91. [CrossRef]
32. Ye, F.; Li, H.; Yu, H.; Chen, S.; Quan, X. Constructing $BiVO_4$-Au@CdS photocatalyst with energic charge-carrier-separation capacity derived from facet induction and Z-scheme bridge for degradation of organic pollutants. *Appl. Catal. B* **2018**, *227*, 258–265. [CrossRef]
33. Sivakumar, S.; Thangadurai, T.D.; Nataraj, D. Role of interfacial AuNPs in solid-state direct Z-scheme MoS_2/Au/g-C_3N_4 heterojunction nanocomposite's pollutant degradation activity under sunlight. *Colloids Surf. A* **2023**, *667*, 131365. [CrossRef]
34. Xiao, X.; Wei, J.; Yang, Y.; Xiong, R.; Pan, C.; Shi, J. Photoreactivity and mechanism of g-C_3N_4 and Ag Co-modified Bi_2WO_6 microsphere under visible light irradiation. *ACS Sustain. Chem. Eng.* **2016**, *4*, 3017–3023. [CrossRef]
35. Gao, B.; Pan, Y.; Chang, Q.; Xi, Z.; Yang, H. Hierarchically Z-scheme photocatalyst of {010} $BiVO_4$/Ag/CdS with enhanced performance in synergistic adsorption-photodegradation of fluoroquinolones in water. *Chem. Eng. J.* **2022**, *435*, 134834. [CrossRef]
36. Chen, R.; Qian, L.; Xu, S.; Wan, S.; Ma, M.; Zhang, L.; Jiang, R. In Situ Fabrication of CdS/$Cd(OH)_2$ for Effective Visible Light-Driven Photocatalysis. *Nanomaterials* **2023**, *13*, 2453. [CrossRef]
37. Ren, Y.; Li, Y.; Pan, G.; Wang, N.; Xing, Y.; Zhang, Z. Recent progress in CdS-based S-scheme photocatalysts. *J. Mater. Sci. Technol.* **2024**, *171*, 162–182. [CrossRef]
38. Prasad, C.; Madkhali, N.; Won, J.S.; Lee, J.E.; Sangaraju, S.; Choi, H.Y. CdS based heterojunction for water splitting: A review. *Mater. Sci. Eng. B* **2023**, *292*, 116413. [CrossRef]
39. Yu, Y.; Chen, F.; Jin, X.; Min, J.; Duan, H.; Li, J.; Wu, Z.; Cao, B. Oxygen Vacancies-Rich S-Cheme BiOBr/CdS Heterojunction with Synergetic Effect for Highly Efficient Light Emitting Diode-Driven Pollutants Degradation. *Nanomaterials* **2023**, *13*, 830. [CrossRef]
40. Yang, L.; Wang, J.; Zhang, Y.; Zhou, B.; Tan, P.; Pan, J. Construction of S-scheme BiOCl/CdS composite for enhanced photocatalytic degradation of antibiotic. *J. Mater. Sci. Mater. Electron.* **2022**, *33*, 13303–13315. [CrossRef]
41. Zhang, H.; Wang, Y.; Zhai, C. Construction of a novel pn heterojunction CdS QDs/$LaMnO_3$ composite for photodegradation of oxytetracycline. *Mat. Sci. Semicon. Proc.* **2022**, *144*, 106568. [CrossRef]
42. Ge, L.; Liu, J. Efficient visible light-induced photocatalytic degradation of methyl orange by QDs sensitized CdS-Bi_2WO_6. *Appl. Catal. B* **2011**, *105*, 289–297. [CrossRef]
43. Zhang, Z.; Lin, Y.; Liu, F. Preparation and photocatalytic performance of CdS@Bi_2WO_6 hybrid nanocrystals. *J. Alloys Compd.* **2021**, *889*, 161668. [CrossRef]
44. Su, Y.; Xu, X.; Li, R.; Luo, X.; Yao, H.; Fang, S.; Homewood, K.P.; Huang, Z.; Gao, Y.; Chen, X. Design and fabrication of a CdS QDs/Bi_2WO_6 monolayer S-scheme heterojunction configuration for highly efficient photocatalytic degradation of trace ethylene in air. *Chem. Eng. J.* **2022**, *429*, 132241. [CrossRef]
45. Zhao, B.; Shao, N.; Chen, X.; Ma, J.; Gao, Y.; Chen, X. Construction of novel type II heterojunction WO_3/Bi_2WO_6 and Z-scheme heterojunction CdS/Bi_2WO_6 photocatalysts with significantly enhanced photocatalytic activity for the degradation of rhodamine B and reduction of Cr (VI). *Colloids Surf. A* **2023**, *663*, 131072. [CrossRef]
46. Pan, J.; Liu, J.; Zuo, S.; Khan, U.A.; Yu, Y.; Li, B. Structure of Z-scheme CdS/CQDs/BiOCl heterojunction with enhanced photocatalytic activity for environmental pollutant elimination. *Appl. Surf. Sci.* **2018**, *444*, 177–186. [CrossRef]
47. Wu, X.; Zhao, J.; Wang, L.; Han, M.; Zhang, M.; Wang, H.; Huang, H.; Liu, Y.; Kang, Z. Carbon dots as solid-state electron mediator for $BiVO_4$/CDs/CdS Z-scheme photocatalyst working under visible light. *Appl. Catal. B* **2017**, *206*, 501–509. [CrossRef]
48. Chen, F.; Yang, Q.; Wang, Y.; Zhao, J.; Wang, D.; Li, X.; Guo, Z.; Wang, H.; Deng, Y.; Niu, C.; et al. Novel ternary heterojunction photcocatalyst of Ag nanoparticles and g-C_3N_4 nanosheets co-modified $BiVO_4$ for wider spectrum visible-light photocatalytic degradation of refractory pollutant. *Appl. Catal. B* **2017**, *205*, 133–147. [CrossRef]
49. Chen, X.; Zhao, B.; Ma, J.; Liu, L.; Luo, H.; Wang, W. The BiOBr/Bi/Bi_2WO_6 photocatalyst with SPR effect and Z-scheme heterojunction synergistically degraded RhB under visible light. *Opt. Mater.* **2021**, *122*, 111641. [CrossRef]

50. Hu, Y.; Hao, X.; Cui, Z.; Zhou, J.; Chu, S.; Wang, Y.; Zou, Z. Enhanced photocarrier separation in conjugated polymer engineered CdS for direct Z-scheme photocatalytic hydrogen evolution. *Appl. Catal. B* **2020**, *260*, 118131. [CrossRef]
51. Zhang, M.; Zhang, Y.; Tang, L.; Zeng, G.; Wang, J.; Zhu, Y.; Feng, C.; Deng, Y.; He, W. Ultrathin Bi_2WO_6 nanosheets loaded g-C_3N_4 quantum dots: A direct Z-scheme photocatalyst with enhanced photocatalytic activity towards degradation of organic pollutants under wide spectrum light irradiation. *J. Colloid Interf. Sci.* **2019**, *539*, 654–664. [CrossRef]
52. Li, K.; Chen, M.; Chen, L.; Xue, W.; Pan, W.; Han, Y. Investigating the Performance and Stability of Fe_3O_4/Bi_2MoO_6/g-C_3N_4 Magnetic Photocatalysts for the Photodegradation of Sulfonamide Antibiotics under Visible Light Irradiation. *Processes* **2023**, *11*, 1749. [CrossRef]
53. Nan, R.; Liu, S.; Zhai, M.; Zhu, M.; Sun, X.; Chen, Y.; Pang, Q.; Zhang, J. Facile Synthesis of Cu-Doped ZnO Nanoparticles for the Enhanced Photocatalytic Disinfection of Bacteria and Fungi. *Molecules* **2023**, *28*, 7232. [CrossRef]
54. Wang, Q.; Zhao, Y.; Zhang, Z.; Liao, S.; Deng, Y.; Wang, X.; Ye, Q.; Wang, K. Facile synthesis of Bi_2WO_6/Bi_2MoO_6 Z-scheme heterojunction for dye degradation and Cr (VI) reduction. *J. Mol. Liq.* **2023**, *383*, 122164. [CrossRef]
55. Yavuz, C.; Erten-Ela, S. Solar light-responsive α-Fe_2O_3/CdS/g-C_3N_4 ternary photocatalyst for photocatalytic hydrogen production and photodegradation of methylene blue. *J. Alloys Compd.* **2022**, *908*, 164584. [CrossRef]